Exploring high aspect ratio gold nanotubes as cytosolic agents: structural engineering and uptake into mesothelioma cells

Sunjie Ye[1,3#], Arsalan A. Azad[2#], Joseph E. Chambers[2], Alison J. Beckett[4], Lucien Roach[1], Samuel C. T. Moorcroft[1], Zabeada Aslam[5], Ian A. Prior[4], Alexander F. Markham[3], Louise P. Coletta[3], Stefan J. Marciniak[2]* and Stephen Evans[1]*

Dr. Sunjie Ye, Dr. Lucien Roach, Samuel C. T. Moorcroft, Prof. Stephen Evans
School of Physics and Astronomy
Woodhouse Lane
Leeds, LS2 9JT, UK
Email: s.d.evans@leeds.ac.uk

Dr. Arsalan A, Azad, Dr. Joseph E. Chambers, Prof. Stefan Marciniak
[2] Cambridge Institute for Medical Research
Keith Peters Building
Hills Road
Cambridge, CB2 0XY, UK
Email: sjm20@cam.ac.uk

Dr. Sunjie Ye, Prof. Alexander F. Markham, Dr. Louise P. Coletta
[3] Leeds Institute of Medical Research,
St James's University Hospital,
University of Leeds,
Leeds, LS9 7TF, UK

Dr. Alison J. Beckett, Prof. Ian A. Prior
[4] Institute of Translational Medicine,
University of Liverpool,
Crown Street, Liverpool, L69 3BX

Dr. Zabeada Aslam

[5]School of Chemical and Process Engineering,

University of Leeds,

Leeds, LS2 9JT, UK

#Co-first authors

*Co-senior authors

The generation of effective and safe nanoagents for biological applications requires their physicochemical characteristics to be tunable, and their cellular interactions to be well characterised. Here, the controlled synthesis has been developed for preparing high-aspect ratio gold nanotubes (AuNTs) with tailorable wall thickness, microstructure, composition and optical characteristics. The modulation of optical properties generates AuNTs with strong near infrared absorption. Surface modification enhanced dispersibility of AuNTs in aqueous media and resulted in low cytotoxicity. The uptake and trafficking of these AuNTs by primary mesothelioma cells demonstrated their accumulation in a peri-nuclear distribution where they were confined initially in membrane-bound vesicles from which they ultimately escaped to the cytosol. This represents the first study of the cellular interactions of high-aspect ratio one-dimensional metal nanomaterials and will facilitate the rational design of plasmonic nanoconstructs as cytosolic nanoagents for potential diagnosis and therapeutic applications.

1. Introduction

The past decade has seen continued advances in the engineering of one-dimensional (1D) nanomaterials, e.g. nanotubes, nanowires, nanorods, for biomedical applications. [1-6] One possible use for such materials is phototherapy, which offers the potential to target the killing of cancer cells whilst causing minimal damage to normal tissues. Typically, near-infrared (NIR) light is used because of its superior tissue penetration. [7-8] The utility of nanomaterials for phototherapy depends on their NIR optical absorption for photo-responses, and their surface properties leading to low cytotoxicity and efficient cellular uptake. An important challenge for photo-triggered nanocarriers lies in their cellular confinement within membrane-bound vacuoles.[9] This can limit therapeutic benefit being adversely modifying their optical properties due to agglomeration, [10] or reducing the efficacy of delivering therapeutic payloads by photo-triggered drug release. [11-12] Recent studies have revealed that silicon nanowires with lengths of several micrometres can enter cells via non-endocytic pathways and demonstrate cytosolic distribution. [13] We hypothesised that NIR-active 1D nanomaterials with similar structural parameters might circumvent the drawbacks of vesicular confinement.

Gold nanotubes (AuNTs) represent an intriguing subset of 1D nanomaterials. Their accessible inner cavity can in principle be loaded with drugs,[14, 15] their open ends can be used as gates for controlled drug release, [16] and their lower heat capacity enables better pulse heating for photoacoustic imaging and photothermal therapy. [17] Despite the potential merits of AuNTs, their lack of NIR absorption and our limited understanding of cellular interactions have hindered their exploitation. For example, the pentagonal AuNTs synthesised by Bi *et al* had an absorption peak at 550 nm, which is located out of the NIR window. [18] Previous literature suggests that the large longitudinal axes of the AuNTs (several micrometres) might hinder their use in cell-based applications. [19] Therefore, it is necessary to develop a method for fabricating AuNTs with tailorable properties and efficient cellular penetration. Here, we report a simple

method for engineering AuNTs with tailorable optical properties, based on modifying microstructure through galvanic replacement between a silver nanowire and HAuCl$_4$, at room temperature. Energy-dispersive X-ray spectroscopic (EDX) mapping and compositional analysis were performed to elucidate the mechanism of microstructural modulation. The control of optical properties allowed the creation of AuNTs with absorption in the NIR region, which were modified by thiol-PEG-FITC to modulate dispersiblity and reduce cytotoxicity. Furthermore, multiple imaging approaches, including confocal 3D correlative light-electron microscopy (CLEM) and single-particle tracking analysis, were used to follow cellular uptake and determine the subcellular fate of AuNTs. Moreover, the optically tuned cytosolic AuNTs demonstrated both efficient photothermal conversion and photothermally-induced primary mesothelioma cell killing. This study is the first to report the cellular interactions of high-aspect ratio 1D metal nanostructures and provides valuable insight into the engineering of plasmonic 1D nanosystems for phototherapy as well as cytosol-based diagnosis and therapeutic applications.

2. Results and Discussion

2.1. Synthesis of AuNTs with different wall thicknesses

Template synthesis represents a powerful and generalizable strategy for preparing hollow gold structures.[20] Synthesis through the galvanic replacement of Au precursors with an Ag template provides a method for producing well-defined hollow entities with tailorable structural and optical properties, depending on the adjustment of the ratios of Au/Ag in the reaction system. [21-23] In this work, polyol synthesis was adopted for the preparation of Ag nanowires (AgNWs), which function as templates for producing the AuNTs (**Figure 1**a). The protocol involves the introduction of a silver precursor solution (AgNO$_3$) and capping agent polyvinylpyrrolidone (PVP) into ethylene glycol (EG), which plays dual roles as both a reducing agent and solvent. [24] Ag nanowires were synthesized at a high wire-to-particle ratio, (Figure 1b and S1), and

possessed a diameter of 100±20 nm (Figure S2). These nanowires had a pentagonal cross-section (Inset of Figure 1b), arising from the uniaxial growth along the 5-fold axes of multiple-twinned seeds of Ag decahedra. [19, 24]
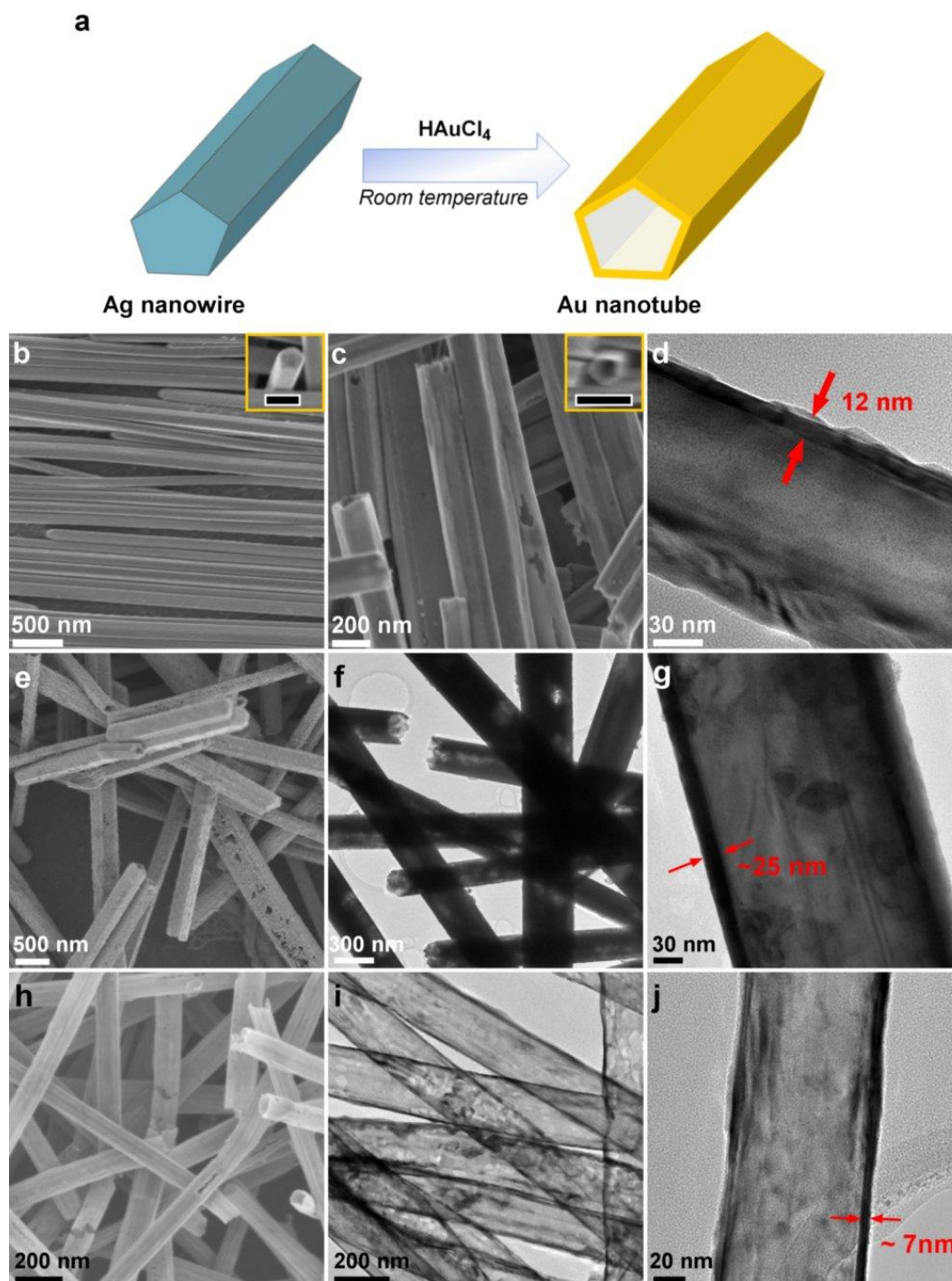

Figure 1. Preparation of AuNTs using AgNWs as templates: (a) schematic illustration of the reaction; (b) SEM image of Ag nanowires, with inset showing pentagonal cross-section (Scale bar in inset: 200 nm); (c) SEM image of AuNTs (synthesised with HAuCl₄ of 2×

stoichiometric amount), with inset showing pentagonal cross-section (Scale bar in the inset: 200 nm); (d) TEM image of an AuNT, with the dark edge showing the wall thickness (red arrows).

Adjustment of the wall thickness of AuNTs: SEM images of AuNTs prepared from AgNWs with the average diameter of (e) 193 nm and (h) 65 nm; Low-magnification TEM images of Au NTs prepared from AgNWs with the diameter of (f) 193 nm and (i) 65 nm; showing a reduced contrast with the increase of diameter; High-magnification of TEM image of Au NTs prepared with the diameter of (g) 193 nm and (j) 65 nm, in which the thickness of each sample can be determined by measuring the dark edge.

AuNTs were prepared via a room-temperature galvanic replacement of gold precursor ($HAuCl_4$) and sacrificial Ag nanowires, capitalizing on the introduction of cetyltrimethylammonium bromide (CTAB).[18] It is generally acknowledged that the formation of hollow gold nanostructures via galvanic replacement needs high reaction temperatures to deliver well-defined morphology, [25] for example, 100°C for PVP-capped Ag nanowires with $HAuCl_4$. [26] CTAB plays essential roles in enabling the preparation of well-defined AuNTs via a room-temperature galvanic reaction, by dissolving AgCl solid and enhancing the inter-diffusion rate between Ag and Au. [25] In addition, CTAB molecules have preferential adsorption onto {100} facets which dominate the side surfaces Ag nanowires, thus leading to the selective deposition of $AuCl_4^-$ onto the side surfaces and eventually the formation of open-ended AuNTs.[18] Scanning electron microscopy (SEM) images of resultant AuNTs (synthesized with $HAuCl_4$ of $2\times$ stoichiometric amounts) demonstrated well-defined tubular structures including an internal cavity, open ends and uniform walls (Figure 1b). Furthermore, these nanotubes assumed structural attributes of the template Ag nanowires, e.g. five straight side edges with a pentagonal cross-section (Inset of Figure 1c). In transmission electron microscopy (TEM) images of individual AuNTs, the edges appeared denser than the central portion owing to the hollow structure of the product. The thickness of the nanotube wall, as represented by the denser edge,

was measured to be ~12 nm. This accords well with previous work that has shown the walls of AuNTs generated using Ag nanowires have wall thicknesses that are one tenth of the Ag nanowires' diameter. [20] This relationship (See details in the Supporting Information) provides a simple mechanism to control wall thickness by adjusting the template. Considering the role of PVP molecules in passivating Ag surface (Figure S4b, See Supporting Information for detailed discussions.), we predicted that Ag nanowire diameter would decrease with increasing PVP concentration. Indeed, varying the PVP concentration from 200, 150, 120 and 100 mM yielded the Ag nanowires with average diameters of 65, 100, 153, 193 nm respectively, with AgNWs formed at a high wire-to-particle ratio in each examined case (Figure 1b, S1- S3). We used Ag nanowires with an average diameter of 65, 100, and 193 nm as templates to prepare AuNTs. Owing to the controllability of the Ag nanowire template diameter (Figure S4a), the wall thickness of AuNTs can thus be tailored between 7 nm to 25 nm, with corresponding inner diameters between 65 nm to 193 nm (Figure 1). This is the first report of a protocol to fine-tune AuNT wall thickness via a solution-phase method (See Supporting Information.). Altered wall thickness may affect the mechanical properties of AuNTs. For example, STEM images of AuNT with a wall thickness of ~ 7 nm showed bending in acute angles without fracture, indicating high flexibility (Figure S5).

2.2. Microstructural modulation of AuNTs

Intriguingly, we also found that the morphology of the final AuNTs was largely dependent on the amount of $HAuCl_4$ added into the reaction system. At the stoichiometric amount of $HAuCl_4$, the products exhibited a tubular structure with alternate darker and lighter banded regions on the wall. (**Figure 2**a and d). When the amount of $HAuCl_4$ was doubled, nanotubes displayed uniform and smooth walls (Figure 2b and e). When $HAuCl_4$ of 3× stoichiometric amount was used, the tubular structures obtained possessed pinholes associated with the walls and small nanoparticles attached on the surface (Figure 2c and f). Partial fragmentation of the nanotube

was also observed resulting in this distinct morphology. It is important to note that the structural evolution with the increased amount of HAuCl$_4$ appeared to follow a pathway distinct from that for the reaction of PVP-capped Ag nanowires with HAuCl$_4$ at 100°C. [26]
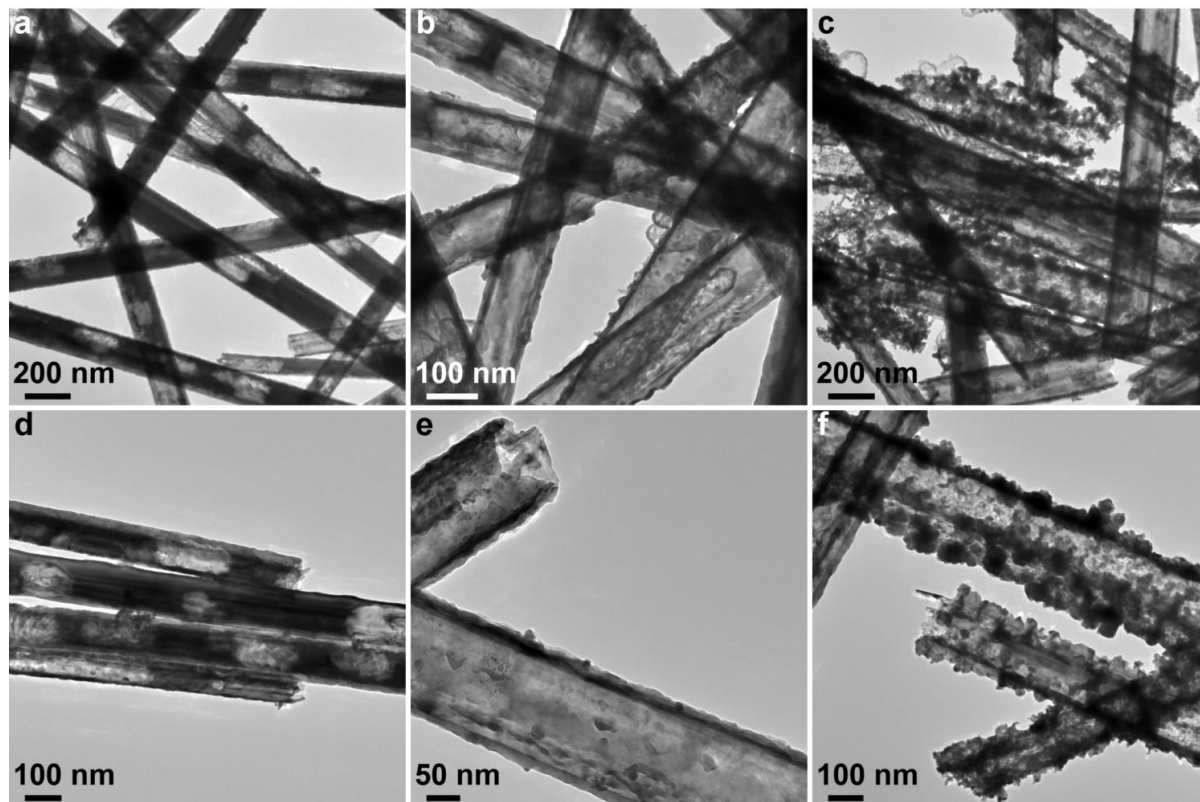

Figure 2. AuNTs prepared with AgNWs (Average diameter: 100 nm) and varying HAuCl$_4$ amount demonstrate different microstructures. HAuCl$_4$ of stoichiometric amount (see Experimental section): (a) Low- and (d) high-magnification TEM images; HAuCl$_4$ of 2× stoichiometric amount: (b) Low- and (e) high-magnification TEM images; HAuCl$_4$ of 3× stoichiometric amount: (c) Low- and (f) high-magnification TEM images.

To better understand the mechanism of these observed differences in the microstructure of nanotubes we collected EDX maps of the elemental distribution (**Figure 3**). For nanotubes synthesised with the stoichiometric amount of HAuCl$_4$, the map of Au element showed a homogenous and seamless layer (Figure 3a). Conversely, that for the Ag element showed regions of negligible contrast in agreement with the dark areas in the high-angle annular dark-

field scanning transmission electron microscopic (HAADF-STEM) image, which corresponded to the vacancies of Ag element. Notably, the overlay of Au and Ag suggested a clear profile of Au element along the tubular structure, indicating the epitaxial deposition of gold atoms on the surfaces of the silver template. The nanotubes synthesised with $HAuCl_4$ of 2× stoichiometric amount displayed intact smooth boundaries and homogeneous elemental distributions in HAADF-STEM images (Figure 3b). Co-localization of Au and Ag was observed in the overlay image, revealing the nanotube wall to be composed of Au-Ag alloy. In HAADF-STEM images of individual nanotubes synthesised with 3× stoichiometric amounts of $HAuCl_4$, the Au and Ag element maps demonstrated structures with rough surfaces coupled with pores in the wall of irregular shapes and sizes (Figure 3c). The overlay image showed the convergence of Au and Ag signals, with no phase segregation observed either for the nanotube wall nor the small nanoparticles attached onto the surface. This indicated that Au and Ag were present in the form of an alloy.

We also conducted atomic absorption spectroscopy (AAS) measurements of nanotube dispersions to investigate the compositional variation of nanotubes synthesized with varying $HAuCl_4$ amounts. In all cases examined, nanotubes were composed of Au and Ag. The mass percentage of Au increased as $HAuCl_4$ was increased from 1x to 2x stoichiometric amount and exhibited a quasi-plateau in the range from 2x to 3x stoichiometric amount. The EDX and AAS results together enabled us to elucidate the formation mechanism and identify the reaction pathway for each sample depicted in Figure 4.
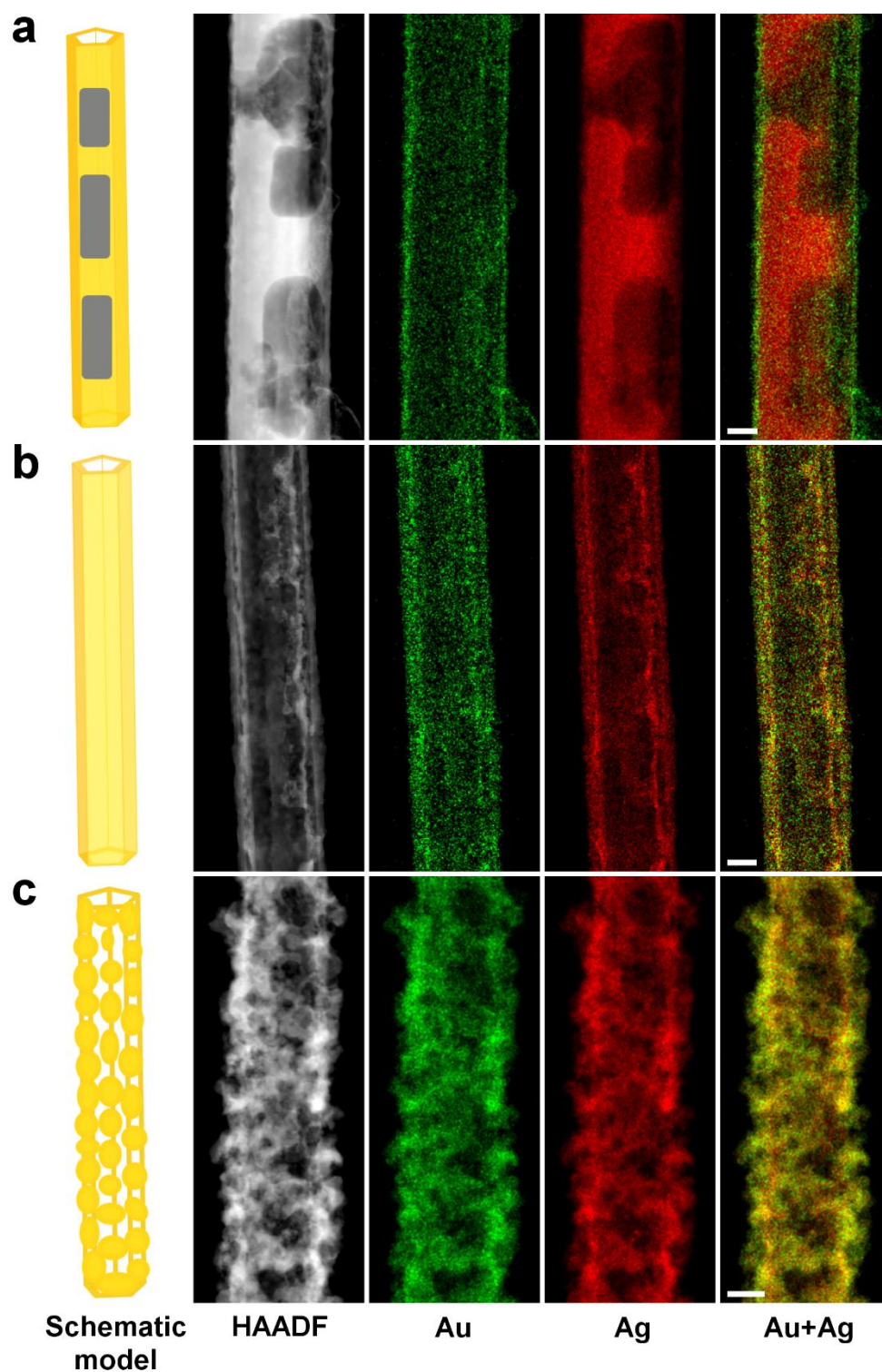
Figure 3. AuNTs prepared with varying HAuCl₄ amount exhibit different patterns of compositional distribution. Schematic model, HAADF-STEM image and EDX mapping of AuNTs synthesized with HAuCl₄ of (a) stoichiometric amount; (b) 2× stoichiometric amount; (c) 3× stoichiometric amount. All scale bars represent 50 nm.

It is noteworthy that Sun *et al.* previously conducted a comprehensive mechanistic study of the replacement reaction between $HAuCl_4$ and PVP-capped silver nanostructures at 100°C, via the titration of silver nanostructures with a $HAuCl_4$ solution, with varying volumes of the $HAuCl_4$ solution (1 mM). [26] Our work, by contrast, focusses on the replacement reaction at room temperature, and highlights the modulation of the microstructure by altering the amount of $HAuCl_4$ added to the reaction system in a single step.

With the addition of $HAuCl_4$ at a stoichiometric amount, the reaction proceeds in two distinct steps: (I) The displacement between Ag and $AuCl_4^-$ ions initially produces Au atoms that form patches on the surface of the silver template via epitaxial deposition. This results from the good lattice matching between Au and Ag; the face-centred cubic crystalline structures for Au and Ag having a lattice constant 4.0786Å and 4.0862 Å respectively. (II) A corrosion process follows with the oxidation of Ag providing electrons (anode reaction) that migrate to the uncovered surface of the Ag nanowire thereby reducing $AuCl_4^-$ into Au atoms (cathode reaction). As a result, an intact Au layer was formed with Ag voids present at the initial reaction sites, creating a tube-like structure with a partially hollow cavity (Figure 2a and 3a). [25]

In the system with $HAuCl_4$ 2× stoichiometric amount, the reaction first follows the pathway described in step (I). Higher concentrations of $HAuCl_4$ facilitate the diffusion of $AuCl_4^-$ ions into resulting volume defects in the Ag template enabling the ions to access the newly formed Ag surface. Consequently, the etching of the Ag template via the replacement continues and enlarges the inner cavity. In conjunction with this process, alloying takes place between the epitaxially-deposited Au coating and covered Ag surface, due to the greater stability of homogenous Au-Ag than that of either pristine Au or Ag. The combination of etching and alloying leads to the formation of the nanotubes with a uniform Au-Ag alloy wall and well-defined inner cavity (Figure 2b and 3b).

When $HAuCl_4$ 3× stoichiometric amount was added, the additional $HAuCl_4$ could selectively etch Ag atoms in the Au-Ag alloy wall, resulting in a dealloying process. Previous reports showed that this dealloying process alters the mass percentage of Au (Au%) in the nanotube to ca. 90% and produces large pores (Size > 20 nm) in the wall. [19, 26] Intriguingly, in the present work, the Au% plateaued at approximately 60% from 2x stoichiometric amount onwards (**Figure 4**a). This suggested a lack of a pronounced dealloying, which was also evidenced by the observation of homogenous Au-Ag alloy without elemental segregation (Figure 3c). This difference in the extent of dealloying may have been caused by the enhanced energy barrier of dealloying at the room temperature in comparison with that at 100℃. Therefore, we suggest that the pores in the nanotube wall (Figure 2c and 3c) may result from the atom reconstruction following a modest dealloying process.

2.3. Optical properties, surface modification and cytotoxicity of AuNTs

The tailoring of the microstructure and composition enabled the control of the optical properties of resultant AuNTs. UV-visible spectra were collected from nanotubes with different Au% (31.6%, 44.3%, 59.0% and 62.3%, synthesized with Au amount of 1x, 1.5x, 2.0x and 3.0x stoichiometric amount, respectively) (Figure 4b). The presence of Ag caused a peak in all preparations around 450 nm, although for the Au%=44.3 sample this appeared as a more subtle shoulder. The dominant peak in the wavelength between 600 nm and 1000 nm can be assigned to the transverse plasmon band of Au-Ag tubular nanostructures (Figure 3b). [19, 26] As Au% increased from 31.6% to 59.0%, this peak showed a red-shift from 620 nm to 926 nm. The peak shift was mainly ascribable to the enlargement of the inner cavity, corresponding to the microstructural evolution from a partially hollow morphology to a well-defined nanotube structure (Figure 2a and 3a). When Au composition was increased to 62.3%, a blue-shift to 700 nm was observed, accompanied by the appearance of a new peak around 550 nm. These spectral

changes may have arisen from the fragmentation of nanotubes, the emergence of Au-Ag alloy nanoparticles on the nanotube surface, as well as the coupling between nanoparticles and nanotube wall. Taken together, AuNTs synthesized with 2× stoichiometric amount exhibited extinction bands well-located in the NIR tissue window (650 nm - 950 nm). We therefore went on to use these in subsequent surface modification and *in vitro* cell studies.
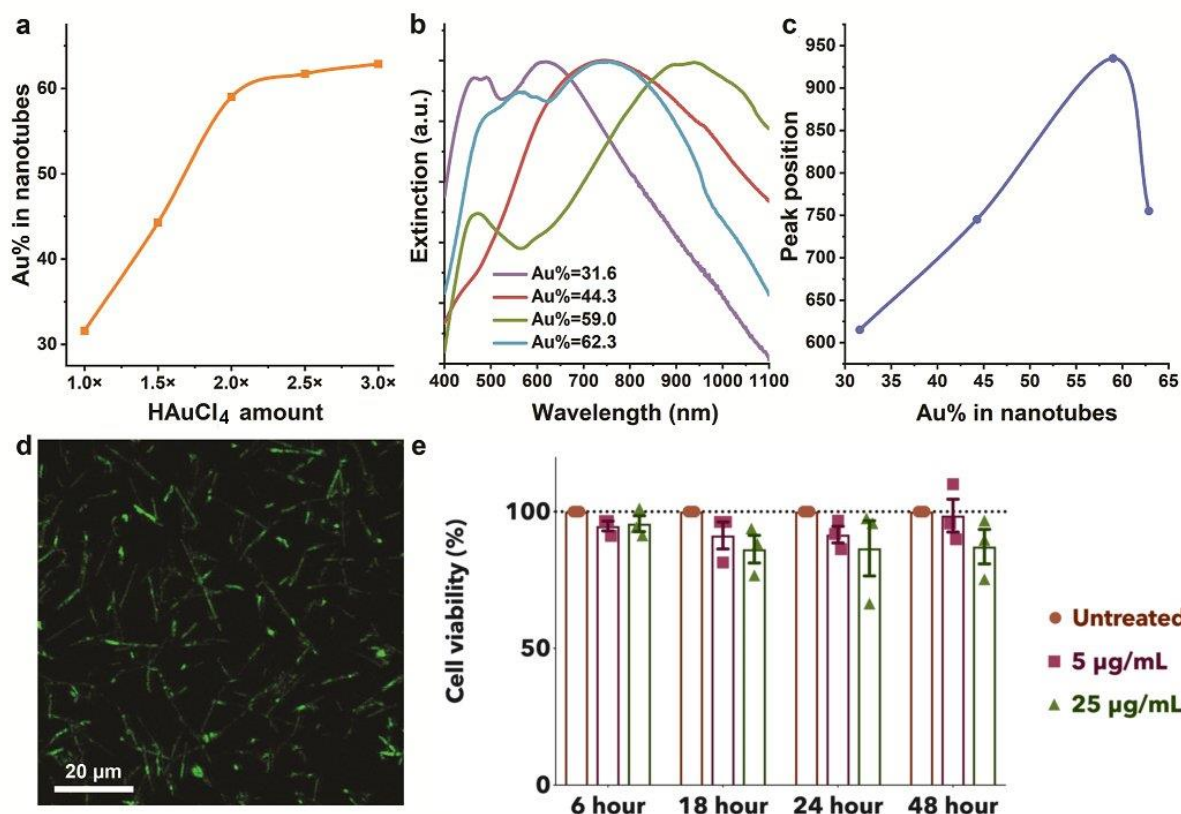

Figure 4. Synthesis of AuNTs with varying HAuCl₄ amount leading to the modulation of optical properties. (a) Plot of Au% in nanotubes (measured by AAS) Vs HAuCl₄ amount relative to stoichiometric amount; (b) UV-vis spectra of AuNTs with different Au% in nanotubes. (c) Plot of the position of dominant absorption peak with Au% in nanotubes (determined by AAS). Surface functionalisation and cytotoxicity assessment of AuNTs: (d) A representative confocal microscopy image of AuNTs after surface modification using Thiol-peg-FTIC (Ex: 495 nm, Em: 520 nm; Scale bar: 20 μm). (e) Cytotoxicity of Meso-7T cells incubated at different concentrations of FITC-AuNTs (Length: 10.1±3.9 µm, inner diameter:

100±20 nm, thickness: ~12 nm, Au%= 59.0%) for 6, 18, 24 and 48 hours. Viability was measured using the CCK-8 assay (n=3).

Although CTAB played a critical role in obtaining well-defined AuNTs at room temperature, the resulting CTAB-AuNTs were prone to severe agglomeration in Mill-Q (Figure S6). Moreover, although the concentration of CTAB required in our protocol is much lower than that of conventional CTAB-mediated seed synthesis of gold nanorods (5 mM vs 100 mM), [27] even low levels of free CTAB are highly cytotoxic and would potentially reduce the biocompatibility of our AuNTs. [28, 29] To resolve the issues of aqueous dispersibility and CTAB toxicity, we carried out surface modification using Thiol-PEG-FITC. Confocal microscopy image of AuNTs after surface modification showed an excellent correlation between the fluorescence signal and gold nanotubes, confirming the successful conjugation of Thiol-PEG-FITC (Figure 4d). Individual nanotubes could be resolved clearly, confirming good dispersibility of FITC-labelled AuNTs in an aqueous medium. Examination of 100 FITC-AuNTs demonstrated a length of 10.1±3.9 μm, an inner diameter of 100±20 nm, a wall thickness of ~12 nm, Au% of 59.0%, and an aspect ratio of ~80 (Figure S7).

Next, we evaluated the cytotoxicity of FITC-AuNTs in primary mesothelioma cells.[30] Malignant mesothelioma is an incurable cancer of the mesothelium caused by exposure to the mineral asbestos.[31] With current standard care, the median survival with mesothelioma is approximately one year and so there is an unmet need for novel targeted therapies. When FITC-AuNTs were incubated for 6, 18, 24 and 48 hours at 5 μg/mL and 25 μg/mL with adherent mesothelioma cells (Meso-7T; MesobanK, UK), no significant cytotoxicity was observed (Figure 4e). The cell viability showed negligible decay with the prolonged incubation time, suggesting good bio-compatibility. Previous studies have reported that, the release of Ag$^+$ ions

from Ag-based nanoagent contributes to strong cytotoxicity, [32, 33] the absence of significant cytotoxicity of our FITC-AuNTs hence indicates their structural integrity and stability in the cellular environment. We postulate this stability in structure and photothermal effect (Figure 8b, to be discussed) arises from the enhanced stability of Au-Ag alloy (the composition of our nanotube wall) compared with that of pure Ag. [26,34]
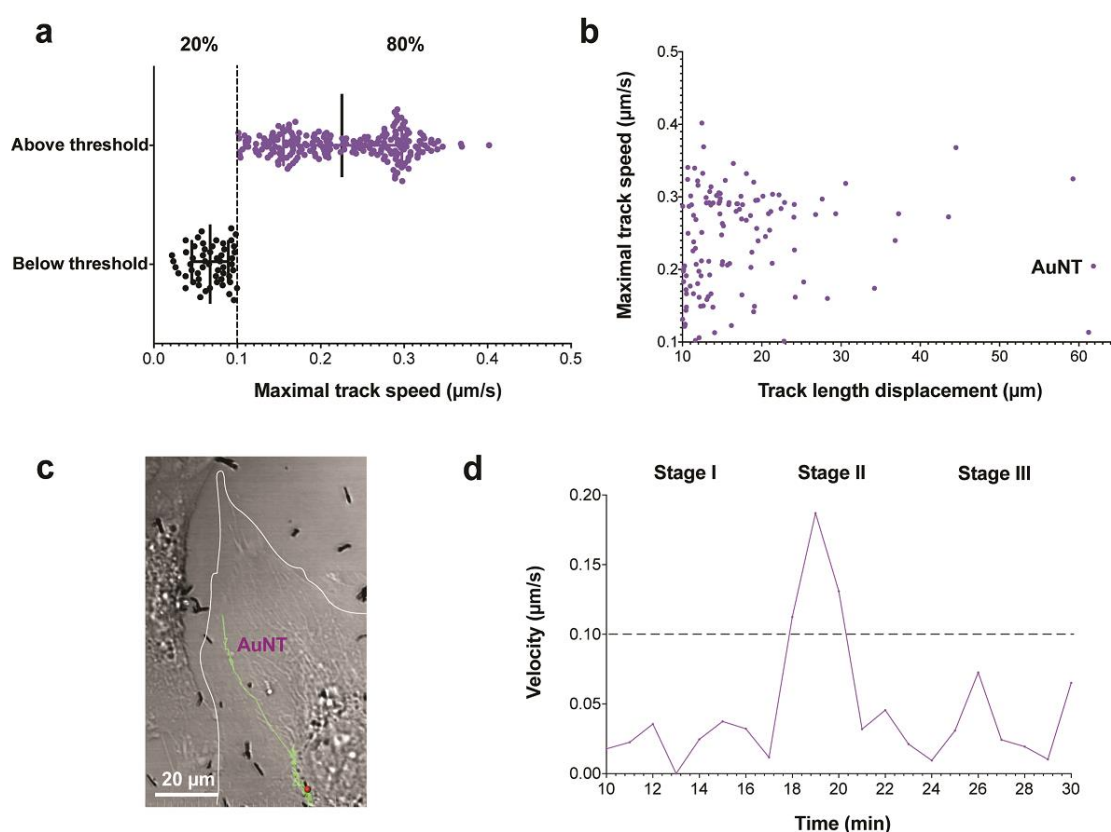

Figure 5. Live cell single-particle tracking of AuNTs in mesothelioma cells. Live-cell uptake of AuNTs in primary mesothelioma (Meso-7T) cells were visualised continuously for 4 hours post-AuNT incubation (Δt=30 s, total frames=480). (a) 80% (n=221) of all identifiable tracks were deemed above the published maximal track speed threshold for nanoparticle active uptake events (0.1 μm/sec[13]). (b) Scatter plot of the 221 maximal track speeds and track length displacement of 10 μm above was then used to identify fast-moving particles traversing over $1/10^{th}$ of the average Meso-7T cell diameter (99.5±22.6 μm, n=20 cells, Table 1). (c) Full-length

track trajectory of the AuNT 010 uptake into a Meso-7T cell. Scale bar represents 20 μm. (d) AuNT 010 transport displays characteristic three-stage uptake mobility: (Stage I) low motility movement representing AuNT bound to the surface of the cell; (Stage II) high-motility linear-trajectory movement representing AuNT vesicular confinement and active transport to the peri-nuclear region (see Video S1); (Stage III) low-motility movement either confined within an organelle or free in the cytosol at the peri-nuclear region.

2.4. Live cell single-particle tracking of AuNTs in mesothelioma cells.

Having established that FITC-AuNTs had appropriate physical, optical and cytotoxicity attributes to serve as PTCAs, we then examined their interaction with primary mesothelioma cells. Mesothelioma cells were plated at 20% confluence and cultured for 24 hours, then AuNTs were added after sonication for 10 seconds to prevent agglomeration. Time-lapse movies were acquired over 4 hours from the point of AuNT addition (Δt=30 s, total frames=480) and AuNTs were visualised using optical reflectance (Figure 5). [13, 35] Dynamics of the AuNTs were analysed by single-particle tracking.

To determine if AuNTs were actively trafficked within mesothelioma cells, a threshold of maximal track speed and track length displacements were used to identify active AuNT uptake events. Of all identifiable tracks, 80% (n=221) were above previously reported maximal track speeds for active-uptake events, for similar aspect ratio nanoparticles (0.1 μm/sec [13]) (**Figure 5**a). To obtain robust data, from these 221 tracks we chose those with track-length displacements of at least 10 μm (Figure 5b), which is 10% of the diameter of a typical mesothelioma cell (99.5±22.6 μm, n=20 cells, Table 1). A typical AuNT track trajectory is shown (Figure 5c and 5d). AuNT transport displayed the characteristic three-stage uptake mobility as has been seen for the active transport of other nanoparticles:[13] (Stage I) low

motility as AuNTs bind to the cell surface; (Stage II) high-velocity linear movement as AuNTs are transported actively; (Stage III) low-motility movement at the perinuclear region (Figure 5d and Supplementary Video S1). This three-stage feature is consistent with reported results for DNA-coated gold spherical nanoparticles (fPlas-gold NPs, gold core: ~ 50 nm in diameter) [36] and high-aspect ratio silicon nanowires [13] (See Table S1 in Supporting Information). These studies both revealed three-stage transport process: (I) low mobility, (II) high mobility and (III) low mobility. However, the high mobility in Stage (II) was assigned to the confinement in early endosomal vesicles for fPlas-gold NPs, wheareas to the active transport by phagosome for silicon nanowires. Low mobility in Stage (III) was assigned to late endosomes or lysosomes in the perinuclear region for fPlas-gold NPs, whereas to the distribution in the perinuclear region with some nanowires released to the cytosol for silicon nanowires. These differences have motivated us to elucidate the cellular uptake process of our AuNTs, via the combined use of other methodologies.
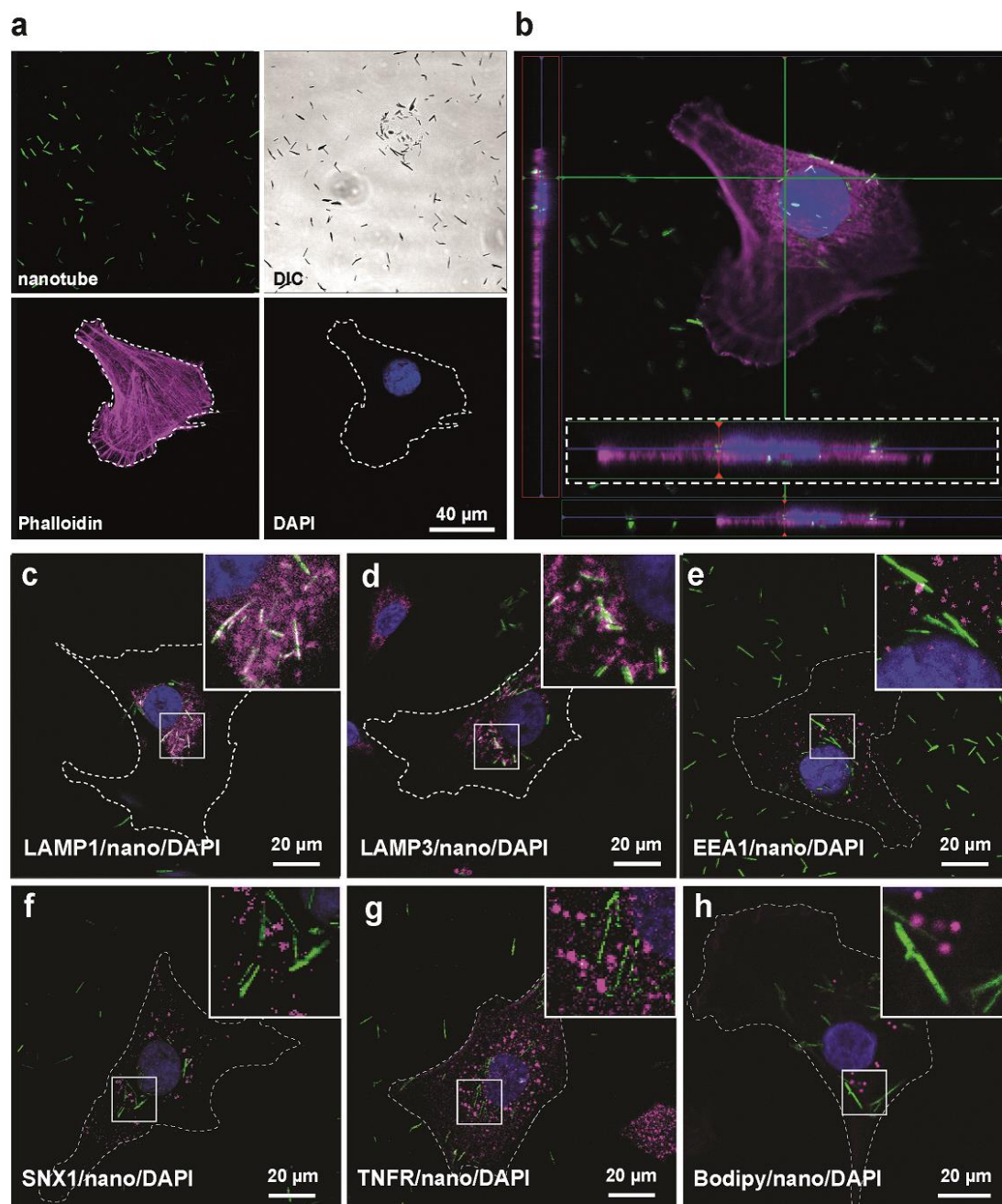
Figure 6. Subcellular fate of AuNTs in mesothelioma cells. (a) Confocal fluorescence image of a mesothelioma (Meso-7T) cell (phalloidin (cell mask), magenta: DAPI (nuclei), blue: DIC), AuNTs were visualised by RCM depending on optical scattering function (in green). Scale bar represents 40 μm. (b) Orthogonal slice demonstrating AuNT internalisation. (c-h) Localisation studies of AuNT with markers for (c) lysosomes (LAMP1), (d) lysosome/late endosomes (LAMP3), (e) early endosomes (EEA1), (f) early sorting endosomes (SNX1), (g) recycling

endosomes (TNFR) and (h) lipid droplets (BODIPY). Nuclei stained with DAPI (blue). Scale bars represent 20 μm.

2.5. Subcellular fate of AuNTs in mesothelioma cells

We then sought to assess the subcellular fate of the AuNTs in mesothelioma cells. Using phalloidin to visualise the F-actin cytoskeleton as a whole-cell mask, intracellular AuNTs were localised predominantly in a perinuclear localisation after 18 hours (**Figure 6**a). Three-dimensional rendering and orthogonal (z-axis) sections confirmed that AuNTs were intracellular (Figure 6b and Supplementary Video S2). Previous studies have variously localised nanoparticles to endosomes, lysosomes or the cytosol. [37, 38] Co-localisation studies were performed by reflectance confocal microscopy (RCM) to visualize AuNTs utilising their optical scattering function (See Experiment Section),[13] and fluorescence confocal microscopy using markers for early endosomes (EEA1), early sorting endosomes (SNX1), recycling endosomes (TNFR) and lipid droplets (BODIPY) (Figure 6c-h). AuNTs demonstrated moderate but incomplete co-localisation with markers for lysosomes (LAMP1) and lysosomes/late endosomes (LAMP3) (Figure 6c-d).

The imperfect co-localisation led us to suspect that at least some AuNTs were not confined within a single class of membrane-bound organelle and so we performed correlative light and electron microscopy (CLEM) of mesothelioma cells exposed to AuNTs for 6 or 18 hours. Cells containing AuNT were identified by live-cell confocal microscopy and then 60 nm slices were generated. At 6 hours following the addition, AuNT could be identified both free in the cytosol (**Figure 7**ai) and confined within vesicular structures (Figure 7aii and Figure S5). In contrast, by 18 hours, AuNT were found exclusively in the cytosol (Figure 7b). In support of AuNT internalisation by endocytosis, at 3 hours peripheral AuNTs can be seen to colocalise with endosomes (Dextran) (Figure S9). Taken together, these results demonstrate that AuNT are internalised and actively transported to the perinuclear region. At least a proportion of the

AuNTs are initially endocytosed but after 18 hours have escaped the endosomal system to reside free in the cytosol.
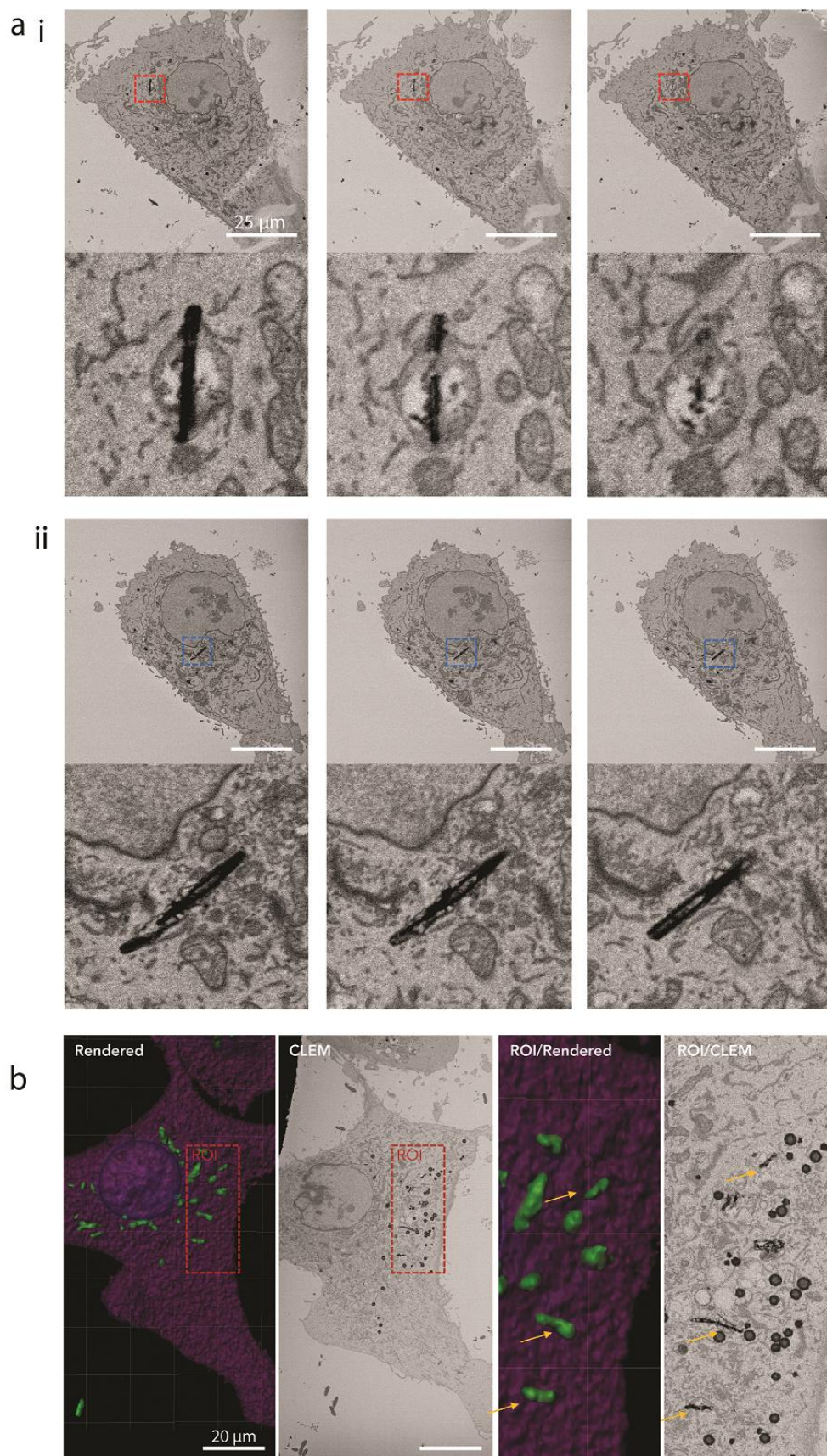
Figure 7. 3D CLEM reveals AuNT vesicular confinement and escape in mesothelioma cells.
3D correlative light electron microscopy (CLEM) was used to determine the subcellular localisation of Au-nanotubes in Meso-7T cells at (a) 6 and (b) 18 hours, respectively. (a) At 6 hours AuNTs demonstrate a mixed distribution, both (a(i)) confined within vesicles and (a(ii)) freely distributed in the cytosol. Bottom left insets show higher magnification of AuNTs of interest. Scale bars represent 25 μm. (b) At 18 hours all AuNTs are freely located within the cytosol. The yellow arrowheads indicate the AuNTs visible in the corresponding EM slice shown in the enlarged region of interest (ROI). Scale bars represent 20 μm.

2.6. Photothermal effect of FITC-AuNTs:

The NIR absorption, negligible cytotoxicity, and cellular internalisation of AuNTs, suggest their potential for use as PTCAs. First, we evaluated their photothermal effects in an aqueous medium (Milli-Q) as a function of AuNT concentration, during the irradiation with a continuous wave (CW) laser at the wavelength of 875 nm with a power density of 1.9 W/cm^2 for 10 mins (**Figure 8**a). The curve for Milli-Q water did not show significant temperature elevation. In contrast, all temperature-time curves for AuNTs of different concentrations displayed a gradual temperature rise, indicative of heat transfer from AuNTs to the solution. The temperature rise is concentration-dependent and the largest temperature change (Δ8.8°C) occurred under for the concentration of 12.5 μg/mL, which would lead to a temperature valid for hyperthermia treatments of cancer therapy (41 to 48°C) based on the body temperature of 37°C.[39] Furthermore, the stability of AuNTs for photothermal heating was investigated by repeating the heating-cooling process for three cycles (Figure 8b). The temperature-time curves demonstrated repeatable profiles of temperature changes, with the largest temperature rise having similar level (ca. Δ8.8°C) after 3 cycles, indicating good photothermal stability of these AuNTs (Figure 8b). The photothermal cytotoxicity of AuNTs was evaluated by exposing mesothelioma cells to a CW laser of 875 nm at a laser density of 1.9 W/cm^2 for 10 mins. (Figure 8c). The laser

irradiation alone did not cause cell death, while with the addition of AuNTs (12.5 μg mL^{-1}), the cell viability upon laser exposure significantly decreased to 50.7% (p<0.01, Figure 8c).

These results reveal that AuNTs in combination with NIR laser irradiation can induce photothermal killing of cancer cells with a low dosage of AuNTs. The observed photothermal effect and cytosol distribution of AuNTs provide the applicability for photothermally-triggered cytosol delivery towards combined photothermal-chemo/gene therapy.
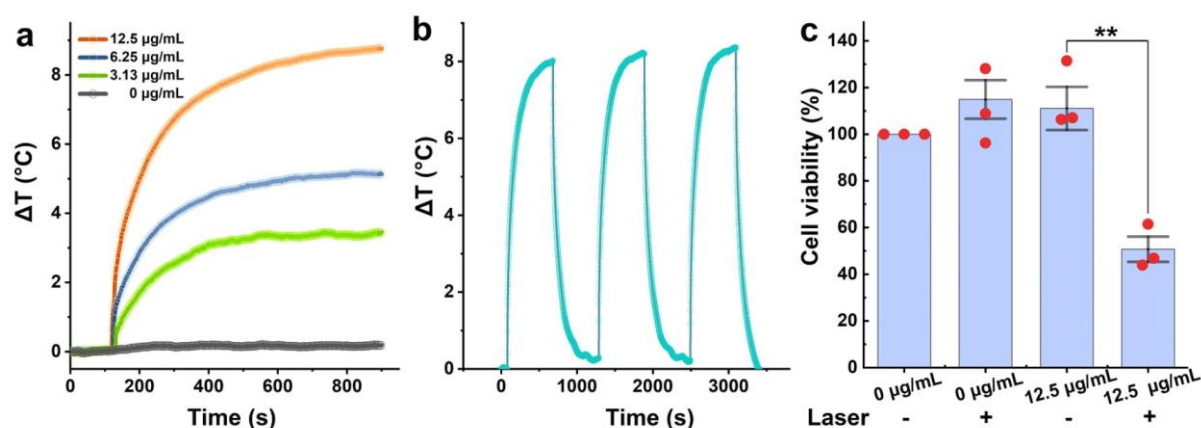

Figure 8. Photothermal effect of FITC-AuNTs: (a) Heating curves of FITC-AuNTs of different concentrations in Milli-Q water, following laser irradiations (Wavelength: 875 nm; irradiation duration: 15 min; laser intensity: 1.9 W/cm^2); (b) Temperature profiles of FITC-AuNTs (12.5 μg/mL) in three successive laser on/off cycles (10 mins of laser exposure followed by 10 mins of laser absence in each cycle) (c) Cell viability after laser exposure: Meso-7T cells were cultured in the medium containing no AuNTs and AuNTs (12.5 μg/mL) and then irradiated with laser (Wavelength: 875 nm, exposure duration: 10 min for each well, laser intensity: 1.9 W/cm^2) Cells in the absence of FITC-AuNTs without laser exposure were used as the control group. Results are shown as mean ±SD (3 technical replicates); ** P<0.01 (unpaired two-tailed Student's t-test).

3. Conclusion

We have explored high-aspect ratio gold nanotubes as cytosolic nanoagents, through robust structural engineering as well as systematical study on the cellular uptake and dynamics. Based on the adjustment of Ag nanowires template in the galvanic reaction, the wall thickness of AuNTs has been tailored via a solution-phase method for the first time. By varying the amount of gold precursor introduced into the galvanic replacement, we have developed an approach to the room-temperature preparation of microstructure-tunable AuNTs. This enables the creation of high-aspect ratio AuNTs with NIR absorption. This approach can be used to construct hollow nanostructures of desirable structural, compositional and optical properties. Consequently, we have engineered NIR-absorbing AuNTs as PTCAs with a broad range of potential application including photothermal cancer therapy and photothermally-triggered drug release. Modification of AuNTs by thiol-PEG-FITC ensured dispersibility in an aqueous medium with low cytotoxicity. The AuNTs were taken up by primary mesothelioma cells and actively transported to the perinuclear region where they eventually escaped vesicular confinement to reside free in the cytosol. The NIR absorption, eventual escape to the cytosol and photothermal properties endow these AuNTs with the potential to be engineered for photo-triggered non-viral delivery of therapeutic molecules. Furthermore, AuNTs with adjustable wall thicknesses could be used to investigate how mechanical properties of nanomaterials affect cellular events, and to develop nanoscale photothermal actuators for manipulating mechanotransduction in living cells. We will explore the capability of our AuNTs for these applications in future work.

4. Experimental Section

Materials: Gold (III) chloride trihydrate (520918), cetyltrimethylammonium bromide (CTAB, H6269), Copper (II) chloride ($CuCl_2$, 203149), sulfuric acid (07208) and ammonium hydroxide solution (NH_3 in H_2O) were purchased from Sigma-Aldrich. Silver nitrate (11414), Polyvinylpyrrolidone (PVP, average M.W. 58,000, A14315) were purchased from Alfa Aesar. Fluorescein PEG Thiol, (FITC-PEG-SH, PG2-FCTH-3k, 3400Da) was purchased from

NanoCS. Ethylene Glycol (EG, 10011073), hydrochloric acid (37%, UN1789) and nitric acid (70%, UN2031) and hydrogen peroxide (H/1750/17) were purchased from Fisher Scientific. Acetone (20066) was ordered from VWR. Milli-Q water (18.2 MΩ·cm at 25°C) was used. All chemicals were used without further purification.

Characterizations: The UV-Vis absorption spectra were recorded with a Perkin-Elmer Model Lambda35 spectrophotometer. SEM micrographs were obtained using a Hitachi SU8230 at a voltage of 2kV. Each SEM sample was prepared by placing 5 µL AgNW or Au NT dispersion (in Milli-Q) onto an aluminum substrate and drying under room temperature naturally. TEM images and energy dispersive X-ray spectroscopy (EDX) mapping results were collected using a range of microscopes at the University of Leeds, a Tecnai F20 TEM/STEM operated at an accelerating voltage of 200 kV, and a Gatan Orius CCD camera running Digital Micrograph software, FEI Titan Themis 300 operated at 300kV fitted with high brightness X-FEG and Supertwin objective lens and a Super-X EDX system with windowless 4-detector design for EDS mapping. (Bright field TEM images were collected with a Gatan OneView 16 Megapixel CMOS digital camera). To prepare samples for TEM imaging, 2 µL AuNT dispersion (in Milli-Q) was dropped onto a carbon-coated copper grid (Agar Scientific Ltd) and dried at room temperature naturally. To measure the elemental Au and Ag contents in the Au NT sample, 200 µL Au NT dispersion was digested in 800 µL aqua regia, diluted with Milli-Q water to 10 mL, and analyzed using using an atomic absorption spectrometer. Confocal microscopy image of FITC-AuNTs (Figure 5a) was collected with a Zeiss LSM880+Inverted/Upright with Airyscan and Leica DM/SP8 Laser Scanning Confocal Microscope. (Ex: 495 nm; Em: 520 nm)
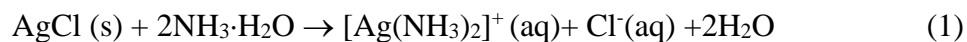
Reaction Preparation: Flasks, vials and stir bars were cleaned with aqua regia (nitric acid and hydrochloric acid in a molar ratio of 1:3) thoroughly rinsed with DI water, and dried in an 80ºC

oven before use. Once dry, the flask and vials were allowed to cool to room temperature before use.

Synthesis of AgNWs: For a typical synthesis, 10 mL of EG was added to round-bottom flask to which a stir bar was added. The flask was then suspended in an oil bath (temperature 152 ℃) and heated for 1 h under magnetic stirring (260 rpm). Concurrent to this heating, reagent solutions were prepared. After 1h heating, $CuCl_2$ solution in EG (4 mM, 80 µL) was injected into heated EG. The solution was then heated for another 15 min. 3 mL of PVP solution in EG (100, 120, 150 or 200 mM, concentration was calculated according to the repeating unit) was then injected into the heated EG, followed by $AgNO_3$ solution in EG (94 mM, 3mL). The reaction was allowed to last for 100 min, and then queched by cooling the reaction flask in a room temperature water bath. Products were then washed with acetone for 3 times by centrigugation (100g* 3 min) and Milli-Q water for 3 times (1000g* 5 min). The AgNW pellet was re-dispersed in 5 mL Milli-Q for future use.

Formation of AuNTs: 1 mL of prepared AgNW (concentration: 2.5mg/mL) was mixed with CTAB aqueous solution (20 mM, 2 mL), and then sonicated for 15 mins. $HAuCl_4$ aqueous solution (difference volume, 10 mM) was slowly added dropwise to the CTAB-AgNW solution. The stoichiometric amount corresponds to 500 µL of 10 mM $HAuCl_4$ aqueous solution. The reaction was then performed at room temperature for 30min and magnetic stirring was used throughout the synthesis. The resultant solution was centrifuged at 1000 g for 3 mins and the supernatant was removed. The pellet was washed with CTAB aqueous solution (10 mM) and $NH_3 \cdot H_2O$ (33%) subsequently, then redispersed in 200 μL $NH_3 \cdot H_2O$ and kept for overnight to further remove the AgCl, according to reaction 1 (some Ag was also removed by treatment with $NH_3 \cdot H_2O$, following reaction 2.[40]). The mixture was centrifuged (1000g, 2 min) and washed with CTAB aqueous solution (10 mM) twice. The final product of Au NTs was redispersed in

Milli-Q.

$$AgCl \text{ (s)} + 2NH_3 \cdot H_2O \rightarrow [Ag(NH_3)_2]^+ \text{ (aq)} + Cl^- \text{(aq)} + 2H_2O \qquad (1)$$

$$4Ag \text{ (s)} + 8NH_3 \text{(aq)} + O_2 + 2H_2O \rightarrow 4[Ag(NH_3)_2]^+ \text{ (aq)} + 4OH^- \text{ (aq)} \qquad (2)$$

Surface Modification with FITC-PEG-SH: the as-prepared Au NTs were added dropwise into the aqueous solution of FITC-PEG-SH (250 µg /mL) in a 1:1 volume ratio and allowed to react for overnight(magnetic stirring was used throughout the reaction) The Au NTs were then collected and washed by centrifugation (1500g*5 min)-redispersion (in Milli-Q) cycle for 3 times to remove free FITC-PEG-SH.

Cell culture: Primary mesothelioma cells (Meso-7T) were obtained from MesobanK (www.mesobank.com). [41] Meso-7T cells were authenticated by Short Tandem Repeat (*STR*) DNA profiling and then cultured in Roswell Park Memorial Institute (RPMI)-1640 growth media supplemented with L-glutamine (2 mM), penicillin (100 U/ml), streptomycin (100 µg/ml), hEGF (20 ng/ml), hydrocortisone (1 µg/ml), heparin (2 µg/ml) and 10% FBS at 37°C and 5% CO_2.

AuNT uptake and subcellular localisation assays: Meso-7T cells were seeded at 80% confluence and cultured for a minimum of 24 hours. AuNTs were then sonicated for 10 seconds and added at a concentration of 25 µg/ml and incubated at 37°C and 5% CO_2 for 18 hours. After 18 hours, the cells were then washed for 3 x 1 minutes with PBS to remove residual AuNTs.

For immunofluorescence, cells were fixed in 4% paraformaldehyde and then permeabilised and blocked with 0.1% Triton X-100 in 2% BSA-PBS. Cell were then incubated with the following primary antibodies at the given dilution: 1:100 anti-LAMP1 (24170 Abcam), 1:100 anti-

LAMP3 (HSB6), 1:100 anti-EEA1 (610457 BioLegend), 1:100 anti-SNX1 (995 Abcam), 1:100 anti-TNFR (82411 Abcam), Alex Fluor-568 Phalloidin (A-12380 Molecular Probes) and Bodipy (D3622) and Dextran (D1863). Cells were then washed 3 x 5 minutes with 1 x PBS and incubated with secondary antibodies (if necessary) Alexa-488, -568 and -647 goat anti-mouse or goat anti-rabbit obtained from Molecular Probes and used at a dilution of 1:400. Finally, cells were washed 3 x 5 minutes with 1 x PBS counterstained with DAPI and then mounted for confocal microscopy. RCM was used to visualize AuNTs as previously reported,[13] as the fluorescence emission of FITC tends to be quenched in low-pH intracelluar envrionment,[42] and our preliminary assesment showed patial detachment of FITC from AuNTs upon cell internalization. During confocal microscopy comprehensive Z-profiles were acquired and reconstructions generated in Imaris, allowing for the 3D visualisation of the distribution of AuNTs within Meso-7T cells.

Correlative light – electron microscopy: Meso-7T cells were plated onto 35mm gridded glass bottom microscopy dishes (MatTek) and treated with AuNTs. The grid coordinates for suitable cells were identified by fluorescence confocal microscopy (Zeiss LSM880). After comprehensive confocal images were acquired of the suitable cells of interest their grid coordinates were recorded using phase contrast for subsequent processing. Cells were then fixed in 2.5% (w/v) glutaraldehyde in 0.1M phosphate buffer (pH 7.4) for serial block face Scanning Electron Microscopy (SEM). Heavy metal staining comprised of reduced osmium (2% (w/v) $OsO4$ +1.5% (w/v) potassium ferrocyanide in ddH_2O), 1% (w/v) thiocarbohydrazide (w/v in ddH_2O), 2% $OsO4$ (w/v in ddH_2O), then 1% (w/v) aqueous uranyl acetate overnight at 4°C. The next day cells were finally stained with Walton's lead aspartate (0.02 M lead nitrate, 0.03 M aspartic acid, pH 5.5) at RT. To prevent precipitation artefacts the cells was washed copiously with ddH_2O between each staining step. Unless stated fixation and staining steps were performed in a Pelco Biowave®Pro (Ted Pella Inc. Redding California, USA) at 100w

20Hg, for 3 mins and 1min respectively. Dehydration was in a graded series of ethanol before filtration and embedding in hard premix resin (TAAB, Reading, UK).

Resin embedded cells were mounted onto cryo pins using conductive silver epoxy and targeted trimming was performed using an ultra-microtome (Leica, Milton Keynes, UK) as previously described. [43] The trimmed block was painted with Electrodag silver paint and coated with 10 nm AuPd using a Q150T sputter coater (Quorum Technologies). Cells were imaged using a Gatan 3View (Gatan, Pleasanton, USA) mounted on a Quanta 250 SEM (FEI, Hillsboro, Oregon, USA) at a resolution of 6 nm in x and y, 75 nm in z. The two-dimensional EM images were then aligned with 3D confocal image reconstructions as described previously.[43] 3D reconstruction of the EM images was performed in Amira.

Single particle tracking: Meso-7T cells were seeded at 20% confluence on a 35mm live-cell images dishes (MatTek) and cultured for a minimum of 24 hours in regular growth medium. The dish was then mounted onto the Zeiss LSM880 equipped with a live cell incubator and a 20X air objective lens to focus on the cell plane. AuNTs were sonicated for 10 seconds and then added at a concentration of 25 µg/ml and cell(s) and AuNT interaction were then immediately imaged continuously for 4 hours (Δt=30 s, total frames=480). AuNTs were tracked using optical reflectance microscopy as previously reported. [13, 35] Following acquisition 320 x 320 µm regions of interest were then cropped and batch analysed using a pre-written macro on Imaris 9.1.

Cytotoxicity assay: To assess cell viability, the formazan-based Cell counting kit-8 (CCK8) reporter assay kit was used according to the manufacturer's instructions (Sigma). In brief, Meso-7T cells were seeded at 5,000 cells per well in a 96-well plate and cultured for 24 hours. The cells were then incubated in a further 100 µl of growth medium containing the appropriate

concentration of AuNTs for 6 or 18 hours. After incubation with AuNTs, cells were further incubated with 10 µl of sterile CCK-8 per well for 1 hour at 37 °C and 5 % CO_2. The optical density was then read for each well at 450 nm using a microplate spectrophotometer. Each experiment was done in triplicate, with three biological repeats.

Photothermal assay: Photothermal heating curves were collected by placing 200 µL of sample dispersion (FITC-AuNTs in Milli-Q water) in individual wells on a 96-well plate, and measuring the temperatures using a thermocouple placed into the well. Neighbouring wells to those containing samples were left empty to provide better thermal insulation, and minimise the rate of heat flow out of the illuminated well (and simultaneously prevent indirect heating of other sample–containing wells). All measurements were taken at a background temperature of 37°C.

For the photothermal assays, Meso-7T cells were seeded into 96-well plates at a density of 5000 cells/well (100 µL medium in each well), and cultured at 37 ºC for 24h. The cells were then incubated with medium containing FITC-AuNTs at the concentration of 0 or 12.5 µg/mL for 18 hours. The cells were exposure to a CW laser (Wavelength: 875 nm, exposure duration: 10 min for each well, laser intensity: 1.9W/cm^2). After the laser exposure, the cells were cultured for 12 hr and 10 µL CCK-8 agent was added in each well, followed by another 3-hr incubation. Cell viability was assessed by measuring absorbance at 450 nm using a microplate reader.

Supporting Information

Supporting Information is available from the Wiley Online Library or from the author.

Acknowledgments

Author Contributions

S.Y. and A.A.A. contributed equally, and S.J.M. and S.D.E. are joint senior authors. S.Y., A.A.A. and J.E.C. designed experiments. S.Y. and A.A.A. performed a majority of experiments, analysed data, and wrote the manuscript with input from other authors. A.J.B. and I.A.P. performed the CLEM experiments and CLEM rendering in Amira. Z.A. collected STEM images and EDX mapping results and assisted in the analysis. L.R. and S.C.T.M collected heating curves and assisted in the photothermal cell assay. L.R. performed AAS measurements. J.E.C., A.F.M. and P.L.C. contributed to the discussion and interpretation of the results and provided critical feedback. S.J.M. and S.D.E. conceived and oversaw the study as a whole and wrote the manuscript.

Conflicts of interest

The authors declare no conflicts of interest.

REFERRENCES

[1] M. R. K. Ali, Y. Wu, Y. Tang, H. P. Xiao, K. C. Chen, T. G. Han, N. Fang, R. H. Wu, M. A. El-Sayed, *Proc. Natl. Acad. Sci. U. S. A.* **2017**, 114, E5655.

[2] X. Z. Chen, M. Hoop, N. Shamsudhin, T. Y. Huang, B. Ozkale, Q. Li, E. Siringil, F. Mushtaq, L. Di Tizio, B. J. Nelson, S. Pane, *Adv. Mater.* **2017**, 29,1605458

[3] M. Hoop, F. Mushtaq, C. Hurter, X. Z. Chen, B. J. Nelson, S. Pane, *Nanoscale* **2016**, 8, 12723.

[4] W. X. Qiu, L. H. Liu, S. Y. Li, Q. Lei, G. F. Luo, X. Z. Zhang, *Small* **2017**, 13, 1603956

[5] W. Zhou, X. C. Dai, C. M. Lieber, *Rep. Prog. Phys*. **2017**, 80, 016701

[6] Z. Mao, Y. Y. Zhang, N. Lu, S. Cheng, R. H. Hong, Q. H. Liu, *Small* **2020**, 16, 1904047

[7] L. Cheng, C. Wang, L. Z. Feng, K. Yang, Z. Liu, *Chem. Rev.* **2014**, 114, 10869-10939.

[8] W. W. Chen, S. H. Zhang, Y. Y. Yu, H. S. Zhang, Q. J. He, *Adv. Mater.* **2016**, 28, 8567-8585.

[9] J. Kim, J. Kim, C. Jeong, W. J. Kim, *Adv. Drug Deliv. Rev.* **2016**, 98, 99-112.

[10] J. Comenge, O. Fragueiro, J. Sharkey, A. Taylor, M. Held, N. C. Burton, B. K. Park, B. Wilm, P. Murray, M. Brust, R. Levy, *ACS Nano* **2016**, 10, 7106-7116.

[11] H. Kim, D. Lee, J. Kim, T. I. Kim, W. J. Kim, *ACS Nano* **2013**, 7, 6735-6746.

[12] Y. Li, W. Hong, H. Zhang, T.T. Zhang, Z. Chen, S. Yuan, P. Peng, M. Xiao, L. Xu, J Control Release 2020.317, 232-245.

[13] J. F. Zimmerman, R. Parameswaran, G. Murray, Y. C. Wang, M. Burke, B. Z. Tian, *Sci. Adv.* **2016**, 2, e1601039.

[14] C. R. Martin, P. Kohli,*Nat. Rev. Drug Discov.* **2003**, 2, 29-37.

[15] R. Tenne, *Nat. Nanotechnol.* **2006**, 1, 103-111.

[16] A. J. Nan, X. Bai, S. J. Son, S. B. Lee, H. Ghandehari, *Nano Lett*. **2008**, 8, 2150-2154.

[17] J. W. Kim, E. I. Galanzha, E. V. Shashkov, H. M. Moon, V. P. Zharov, *Nat. Nanotechnol.* 2**009**, 4, 688-694.

[18] Y. P. Bi, G. X. Lu, *Nanotechnology* **2008**, 19. 275306.

[19] Y. G. Sun, *Nanoscale* **2010**, 2, 1626-1642.

[20] Y. G. Sun, B. T. Mayers, Y. N. Xia, *Nano Lett*. **2002**, 2, 481-485.

[21] N. R. Sieb, N. C. Wu, E. Majidi, R. Kukreja, N. R. Branda, B. D. Gates, *ACS Nano* **2009**, 3, 1365-1372.

[22] A. M. Goodman, Y. Cao, C. Urban, O. Neumann, C. Ayala-Orozco, M. W. Knight, A. Joshi, P. Nordlander, N. J. Halas, *ACS Nano* **2014**, 8, 3222-3231.

[23] B. Goris, L. Polavarapu, S. Bals, G. Van Tendeloo, L. M. Liz-Marzan, *Nano Lett*. **2014**, 14, 3220-3226.

[24] K. E. Korte, S. E. Skrabalak, Y. N. Xia, *J. Mater. Chem.* 2008, 18, 437-441.

[25] E. Gonzalez, J. Arbiol, V. F. Puntes, *Science* **2011**, 334, 1377-1380.

[26] Y. G. Sun, Y. N. Xia, *J. Am. Chem. Soc.* **2004**, 126, 3892-3901.

[27] X. C. Ye, L. H. Jin, H. Caglayan, J. Chen, G. Z. Xing, C. Zheng, V. Doan-Nguyen, Y. J. Kang, N. Engheta, C. R. Kagan, C. B. Murray, *ACS Nano* **2012**, 6, 2804-2817.

[28] L. Vigderman, P. Manna, E. R. Zubarev, *Angew. Chem. Int. Ed.* **2012**, 51, 636-641.

[29] Y. Zhang, B. Newton, E. Lewis, P. P. Fu, R. Kafoury, P. C. Ray, H. T. Yu, *Toxicol. In Vitro* **2015**, 29, 762-768.

[30] *T. Chernova, X. M. Sun, I. R. Powley, S. Galavotti, S. Grosso, F. A. Murphy, G. J. Miles, L. Cresswell, A. V. Antonov, J. Bennett, A. Nakas, D. Dinsdale, K. Cain, M. Bushell, A. E. Willis, M. MacFarlane, Cell death differ.* **2016**, 23, 1152-1164.

[31] M. Carbone, B. H. Ly, R. F. Dodson, I. Pagano, P. T. Morris, U. A. Dogan, A. F. Gazdar, H. I. Pass, H. N. Yang, *J. Cell. Physiol.* **2012**, 227, 44-58.

[32] S. G. Lehmann, D. Toybou, A. E. P. del Real, D. Arndt, A. Tagmount, M. Viau, M. Safi, A. Pacureanu, P. Cloetens, S. Bohic, M. Salome, H. Castillo-Michel, B. Omana-Sanz, A. Hofmann, C. Vulpe, J. P. Simonato, C. Celle, L. Charlet, B. Gilbert, *Proc. Natl. Acad. Sci. U. S. A* **2019**, 116, 14893-14898.

[33] J. Y. Liu, Z. Y. Wang, F. D. Liu, A. B. Kane, R. H. Hurt, *ACS Nano* **2012**, 6, 9887.

[34] H. Z. Shi, L. D. Zhang, W. P. Cai, *J. Appl. Phys.* **2000**, 87, 1572-1574.

[35] J. F. Zimmerman, G. F. Murray, B. Z. Tian, *J. Phys. Chem. C* **2015**, 119, 29105-29115.

[36] M. M. Liu, Q. Li, L. Liang, J. Li, K. Wang, J. J. Li, M. Lv, N. Chen, H. Y. Song, J. Lee, J. Y. Shi, L. H. Wang, R. Lal, C. H. Fan, *Nat. Commun.* **2017**, 8. 15646.

[37] S. Behzadi, V. Serpooshan, W. Tao, M. A. Hamaly, M. Y. Alkawareek, E. C. Dreaden, D. Brown, A. M. Alkilany, O. C. Farokhzad, M. Mahmoudi, *Chem. Soc. Rev.* **2017**, 46, 4218-4244.

[38] J. Mosquera, I. Garcia, L. M. Liz-Marzan*,* **2018**, 51, 2305-2313.

[39] D. Jaque, L. M. Maestro, B. del Rosal, P. Haro-Gonzalez, A. Benayas, J. L. Plaza, E. M. Rodriguez, J. G. Sole, *Nanoscale* **2014**, 6, 9494-9530.

[40] S. E. Hunyadi, C. J. Murphy, *J. Mater. Chem.* **2006**, 16, 3929-3935.

[41] R. C. Rintoul, D. M. Rassl, J. Gittins, S. J. Marciniak, K. C. Mesoban, *Thorax* **2016**, 71, 380-382.

[42] A. K. Chen, Z. L. Cheng, M. A. Behlke, A. Tsourkas, *Anal. Chem.* **2008**, 80, 7437-7444.

[43] D. G. Booth, A. J. Beckett, O. Molina, I. Samejima, H. Masumoto, N. Kouprina, V. Larionov, I. A. Prior, W. C. Earnshaw, *Mol. Cell* **2016**, 64, 790-802.